Int J Adv Manuf Technol (2017) 92:231–245
DOI 10.1007/s00170-017-0129-0

ORIGINAL ARTICLE

Online detection method of weld penetration based on molten pool morphology and metallic vapor radiation for fiber laser welding

Jie Sheng[1] · **Yan Cai**[1,2] · **Fang Li**[1,2] · **Xueming Hua**[1,2]

Received: 1 November 2016 / Accepted: 3 February 2017 / Published online: 22 February 2017

Abstract A novel detection method of penetration status was presented for a high-power fiber laser welding. The metallic vapor and molten pool was recorded by a high-speed camera during welding process. The radiation intensity of metallic vapor, as well as the morphology of molten pool end, was calculated by image processing algorithm as image features. Four image features, the radiation intensity of metallic vapor (RIMV), the area of molten pool end (AMPE), the rear angle of molten pool end (RAMPE), and the aspect ratio of molten pool end (ARMPE), were extracted. The mean value, relative range, variation coefficient, and frequency ratio were computed for the four features to obtain the 16 characteristic parameters. Aiming at penetration status, the characteristic parameters were reorganized to form two complex indicators by the principal component analysis. Experimental results showed that the detection method was potential for online detection on the penetration status in a high-power laser welding process.

Keywords Fiber laser welding · Penetration status · Detection method · Principal component analysis

✉ Yan Cai
ycai@sjtu.edu.cn

[1] Shanghai Key Laboratory of Materials Laser Processing and Modification, Shanghai Jiao Tong University, Shanghai 200240, China

[2] Collaborative Innovation Center for Advanced Ship and Deep-Sea Exploration, Shanghai 200240, China

1 Introduction

Fiber laser welding showed unique advantages in joining medium-thick steel plates, including a high depth-to-width ratio, narrow heat affected zone, and small welding deformation. Compared with a thin plate, the stability and consistency of welding process is more important and difficult to keep for a thick plate. In particular, penetration fluctuation is a typical problem that impedes the extensive application of a high-power laser in heavy industry to some extent. In recent years, many studies were reported on the online monitoring methods or controlling technology of penetration for laser welding process.

Bagger et al. [1] utilized a photoelectric sensor mounted on the back side of the plate to detect penetration status. The even penetration was obtained at the lapping zone with the adjustment based on this sensor. However, the detection method from the back side was limited inevitably, especially in industrial applications. In recent years, some investigations were carried out to obtain penetration information from the top side, normally based on a molten pool or keyhole. The drastic eruption of metallic vapor and strong optic radiation makes it difficult to observe during a high-power laser welding. In order to obtain effective information, many novel methods were designed based on various sensors and analysis algorithm. You et al. [2] devised a multiple-sensor detection system to detect imperfection formation during disk laser welding. Kim et al [3] devised a specific coaxial cameral system to observe the morphology of a keyhole and molten pool in a laser remote welding. Some image processing methods were also used to extract information. An image processing algorithm was designed by Gao et.al [4] based on a gray character to extract the edge of a molten pool and a keyhole in laser welding. Zhang et al. [5] predicted the weld seam width and height by

measuring the welding pool shadow. Luo et.al [6] extracted the welding pool edge and characterized the width of weld seam accordingly.

Although the detection method for penetration from the top side is indirect, it was proved by many studies to be effective and easy to implement. Özmert et al [7] showed that there was a certain relationship between the penetration depth and the width as well as the length of welding pool. Kratzsch et al [8] investigated the relationship between the gray feature of the keyhole image and the penetration depth. It showed that when it is fully penetrated, a lower brightness zone inside the keyhole, called as full penetration hole (FPH), would appear. Abt et al. [9] and Blug et al [10] designed closed-loop control systems of penetration status and laser power according to the existence and the size of the keyhole, respectively. Shidfar et al. [11] calculated the weld penetration by detecting the temperature distribution in the vicinity of molten pool. The preceding research work provided references from the aspects of interaction mechanism and observation means. However, it was quite difficult to implement because of the complicated devices and algorithm. An effective, efficient, and low-cost method to monitor weld penetration was still urgent for a high-power laser welding.

In view of the abundant information and complex features of molten pool during laser welding, this paper proposed an online detection system for weld penetration based on the principal component analysis (PCA) technology. The rear profile of molten pool, as well as the radiation of metallic vapor, was recorded during a fiber laser welding process. Four static features were extracted from the perspective of the morphology of molten pool and its interaction with metallic vapor and keyhole. As far as the continuous welding process, four process parameters were designed for every aforementioned static feature. Accordingly, there were total 16 process parameters to describe a fiber laser welding process. With the PCA, two complex indicators were established to estimate the penetration status of laser weld with varied laser power and plate thickness. Experiment results indicated that the weld penetration could be detected by the pair of indicators effectively. With the proposed method, the direct observation of the keyhole, as well as the computation of molten pool's temperature field, was no longer obligatory. The complexity and cost of observation system was greatly reduced. The decrease of computation made online monitoring possible. The evaluation results could be obtained within 3–10 s after completion of welding.

2 Experimental system

Figure 1 illustrated a schematic diagram of the experimental layout employed during these experiments. The experimental system consisted of IPG fiber laser welding equipment, a shielding gas (Argon) device, a 6-axis robot arm, and a welding experimental platform equipped with a high-speed camera, motor servo, and fixing devices. The maximum output power of fiber laser source was 10 kW, and the corresponding focus diameter was 0.3 mm. The working head was stationary during the welding process, and the platform, on which the workpiece was fixed, moved at a constant speed along the length direction of a web plate. The gas nozzle was located in a leading direction.

The camera, with a macro lens and a band pass filter (808 nm), was mounted at the welding platform. The image of welding zone was taken from behind, focusing at the end of molten pool. The angle between the optical axis of the camera and the central line of the incident laser was 45°. The shooting speed was 1362 fps. The distance between the camera bottom and the top surface of platform was about 630 mm.

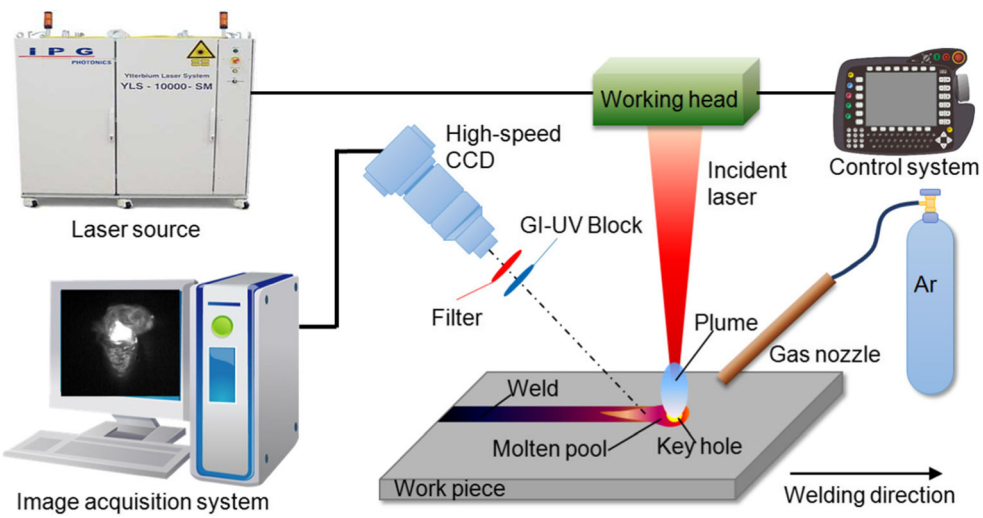

Fig. 1 Schematic diagram of experimental equipment and image acquisition system

The material used in this study was low carbon steel for shipbuilding, and the dominant element was iron with 0.16% C, 0.22% Si, 0.58% Mn, 0.019% S, and 0.013% P. The sample size was 200 mm (L) × 200 mm (W), but the thickness was divided into two types, 6 and 8 mm. All sample surface and edges were carefully milled and cleaned with a high-purity acetone.

In order to observe the molten pool in different penetration status, the welding samples were divided into three groups, as shown in Fig. 2. The welds of group I were fully penetrated, while the other two groups were partially penetrated. Besides the laser power, the other welding parameters are fixed. The welding speed was 1 m/min, while the defocusing distance was −6 mm. The gas flow rate was 20 L/min. Welding speed is fixed at 1 m/min for all groups.

There were six welds in each group. The typical images of cross section were presented in Fig. 3. It could be observed that the full penetration disappeared when laser power decreased or steel plates were thickened. The weld morphology changed obviously when a lack of fusion occurred, which indicated that the morphology and behavior of molten pool changed with penetration conditions.

3 Welding process analysis

3.1 Metallic vapor and molten pool

As far as high-power laser welding, the keyhole is the most critical factor to determine the weld penetration. The multiple reflection of incident laser in the keyhole has an important effect on the energy transfer [12]. Only when the keyhole penetrated through a welded plate, a full penetration occurred. Normally, the metallic vapor above the workpiece decreased obviously when the keyhole was provided with an upper outlet and a lower outlet at the same time. Accordingly, some scholars have used the metallic vapor to estimate the welding status. However, there are many influence factors on metallic vapor. The detection method based only on light intensity was limited in a very narrow range of applications. The information from molten pool provided an appropriate supplement, since its profile had much close relationship with penetration conditions.

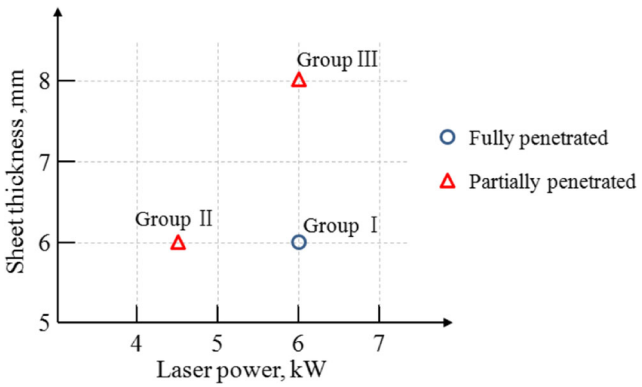

Fig. 2 The grouping of experiments and welding parameters

With the movement of the keyhole during the laser welding process, the liquid metal flowed to the end of molten pool through the sides of the keyhole. Recent research showed that there was a close relationship between penetration conditions and the morphology of molten pool [13].

In the case of partial penetration, the convection in the upper part of molten pool was weak due to the influence of side assisted gas and metallic vapor. Near the bottom of the keyhole, the vapor pressure is perpendicular to the liquid metal, and only the surface tension works as a driving force. Accordingly, the convection in this zone was not strong either. There was only a slow convection circle in molten pool, as shown in Fig. 4a.

The extrusion force and friction force between the metallic vapor and the keyhole wall are the dominant factors to change the profile of a molten pool [14, 15]. When full penetration was established, keyhole penetrated through the thickness of plates, and there were two outlets for metallic vapor to escape, from the top side and bottom side, respectively. The pressure of metallic vapor inside the keyhole dropped dramatically due to the increase in the number of outlets. Accordingly, the convection of molten pool was separated into two circles, as shown in Fig. 4b. The upper circle was depressed by the side assist gas to some extent. The lower convection circle was free from constraint force and still kept a relatively active movement.

As far as the surface of molten pool, the different movements played an important role. In one circle mode, liquid metal mainly moved to the upper part of the workpiece, although the amount of molten metal was less. Accordingly, the end of molten pool showed a slender profile. When the keyhole penetrated through the workpiece, the flow pattern of molten pool changed to the double-circle mode. The upper flow circle led to a plump profile of molten pool. The morphology difference of molten pool was helpful to distinguish the penetration state.

3.2 Image processing

Because the arrangement of the high-power laser welding system, the detection camera was placed obliquely above the incident point of a laser beam. Both the metallic vapor and the molten pool can be recorded in this imaging mode. Due to the angle between the imaging surface of a camera and the surface of the workpiece, the image was compressed obviously in the X direction. Besides, the image was a little distorted in Y direction, because the light axis of the camera was not strictly parallel to the X coordinate. In addition, the camera

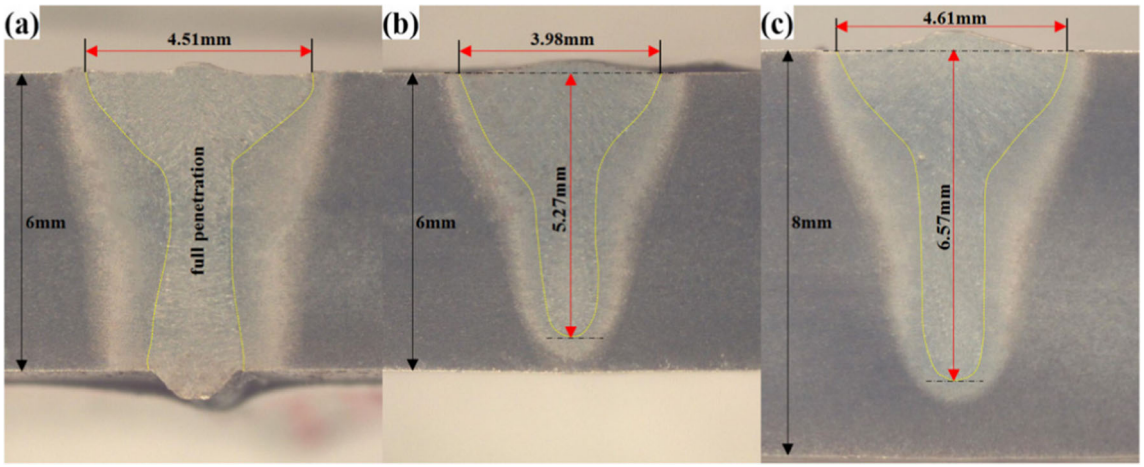

Fig. 3 The typical images of weld cross section. **a** Group I. **b** Group II. **c** Group III

itself also led the barrel distortion to some extent. All the factors decreased the accuracy of subsequent calculations. To this end, a transformation algorithm was used to solve the problem, as shown in Fig. 5. Before welding, a calibration board with a round dot matrix was set on the top surface of the welding sample. The dot diameter was 1.5 mm, and the spacing between adjacent dots was 4 mm. It could be found that the round dot became ellipse, and spacing in X direction was reduced, as shown in Fig. 5a. After distortion correction, the shape of the dot became standard circle, and the distance among dots became even, as shown in Fig. 5b. In the process of welding detection, all images were transformed firstly, as shown in Fig. 5c, d, to eliminate the effects of distortion.

In the transformed image of welding zone, the rear part of molten pool, as well as metallic vapor, could be observed clearly. In order to separate the two targets, an improved Otsu algorithm was used to determine the edge of metallic vapor. The first step was to compute the maximum variance between clusters for the separation of the metallic vapor. Then the similar computation was executed inside the left zone for the molten pool. After the two steps of Otsu calculation, both metallic vapor and molten pool were extracted from the background.

Inside the target zone, the gray gradient of each pixel was calculated in its eight neighborhoods. If the highest gray gradient exceeded the preset threshold value, this point was considered as edge. After all pixels were processed, the distances among the point were computed. The point far away from all other points would be rejected from the edge. The remaining points were connected as the edge of target. Therefore, the profile of metallic vapor, as well as the end of molten pool, was presented in Fig. 6.

3.3 Image features

The static image of molten pool and metallic vapor reflected the welding status of a certain moment. Based on the foregoing analysis, the characteristics were extracted from each image as image features, as shown in Fig. 7a. The four image features are the radiation intensity of metallic vapor (RIMV), the area of

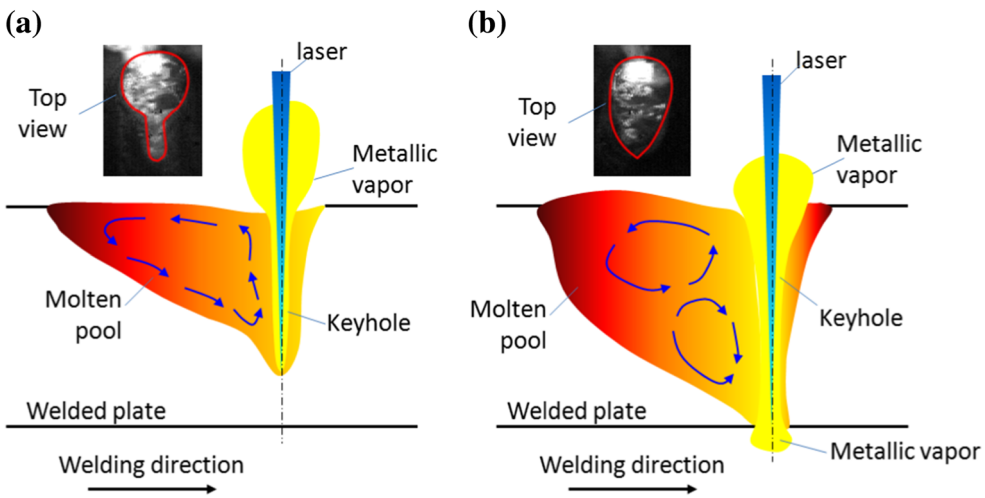

Fig. 4 The sketch map of molten pool's movement. **a** Artial penetration. **b** Full penetration

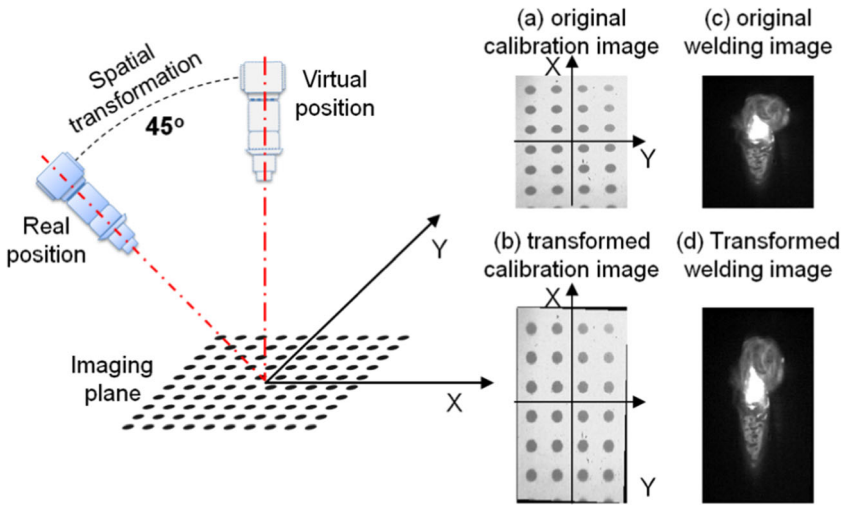

Fig. 5 The sketch map of image transformation and typical images

molten pool end (AMPE), the rear angle of molten pool end (RAMPE), and the aspect ratio of molten pool end (ARMPE). The first parameter was related to the metallic vapor, and the latter three parameters reflected the shape of the molten pool.

Suppose the image size of metallic vapor is $m \times n$. Here, M is the set of pixels of metallic vapor, and its complement set is the background, as shown in Fig. 7b. The RIMV is defined as the gray value average of all pixels inside set M.

$$\mathrm{RIMV} = q \sum_{\substack{0 \le i \le m \\ 0 \le j \le n}} \frac{1}{255} k_{i,j} \cdot g_{i,j}, k_{i,j} = \begin{cases} 1, g_{i,j} \in M \\ 0, g_{i,j} \notin M \end{cases} \quad (1)$$

where $g_{i,j}$ is the gray value of a pixel (i, j) with weighting coefficient of $k_{i,j}$, i, and j indicate the pixel's location of the row and column, respectively. The image segmentation is performed based on the Otsu algorithm and morphologic processing technology. As an adjustment value, q is adopted to attenuate the difference caused by photography system. As far as the comparative analysis based on the same imaging system, the q could be set to 1.

A circle was drawn on the molten pool image with the laser incident point as center, and welded seam width as diameter, as shown in Fig. 7c. On the basis of this virtual circle, the computational domain was established for the end of molten pool. Here, the molten pool located inside the computational domain is called the end part. Based on the extracted profile of molten pool, the area of the shaded zone was defined as the AMPE. There are two intersections, A and B, between the weld pool and the upper edge of the computational domain. Point C is the intersection between the central axis and the profile of molten pool. The RAMPE was defined as the angle between line AC and line BC. The ARMPE is defined as the ratio between the edge AB and the height, H, of triangle ABC.

During laser welding process, molten pool and metallic vapor were always in the state of fluctuation. This is closely related to the interaction characteristics between laser beam and the welded material. A set of continuous images were selected randomly from different experimental groups and presented in Fig. 8. It was observed that both metallic vapor and molten pool varied continuously in all groups, no matter whether the full penetration was established. When the first two groups were taken for comparison, the reduction of laser power not only depressed the metallic vapor, but also narrowed the molten pool. However, the differences between group I and group III were difficult to recognize, since the laser power was same for the two groups. Although group I has full penetration, the bottom open of the keyhole was quite narrow. The bottom width of welded seam was close to that of partial penetration. The small amount of metallic vapor ejected from the bottom open changed the behavior of molten

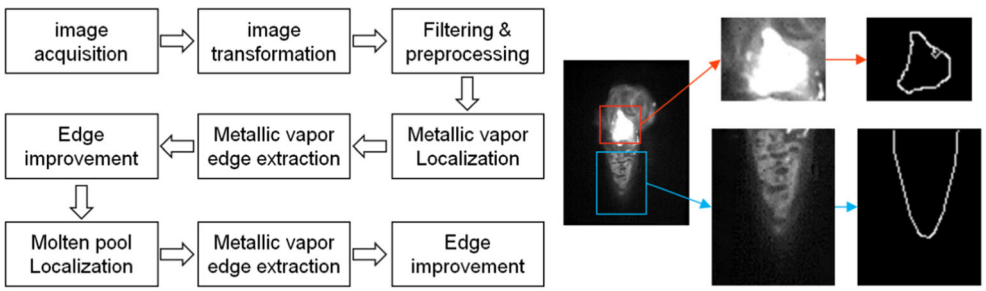

Fig. 6 The flow chart of contour extraction for the molten pool and the metallic vapor

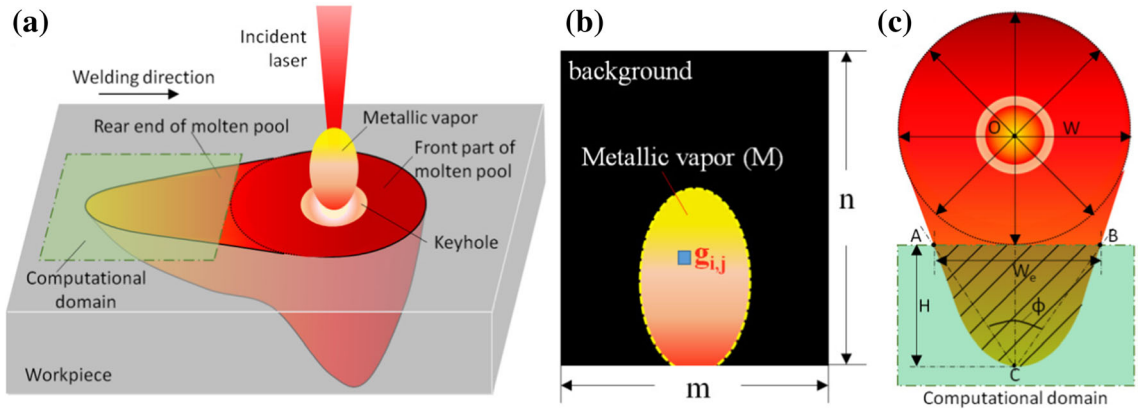

Fig. 7 The static features of molten pool and metallic vapor. **a** General layout of laser welding. **b** Sketch of metallic vapor. **c** Sketch of molten pool

pool and plume. However, the image differences caused by the narrow bottom open were not remarkable. The fluctuation of metallic vapor increased the difficulty of identification. Therefore, it is necessary to analyze all images of the whole welding process and to extract the process parameters.

3.4 Characteristic parameters

The four static features, the RIMV, the AMPE, the RAMPE, and the ARMPE, were calculated during the welding process and shown in Figs. 9, 10, and 11. The weld depth in a longitudinal section was presented correspondingly. It was observed that the image features varied with the development of the welding process for all groups. Even for the full penetration weld, the fluctuation of image features was obvious. This indicated that the interaction between the material and the laser beam had time-varying characteristics. Besides image features, this fluctuation also carried information related to penetration condition. For group I, the image features could be described as random signals within a certain range. For group II and group III, the fluctuation of image features showed a periodic characteristic to some extent, especially on the image features of molten pool. In general, the periodic characteristic of image features became more obvious in partial penetration than that in full penetration. In order to describe the time-varying characteristics, statistical analysis and frequency domain analysis methods were used.

From a statistical point of view, the process parameters were designed including the mean value (M), variation coefficient (CV), and relative range (R).

For a series of data, the (CV) was defined as Eq. (2):

$$CV = \frac{s}{\bar{x}} = \frac{\sqrt{\frac{1}{n-1}\sum_{i=1}^{n}\left(x_i - \bar{x}\right)}}{\frac{1}{n}\sum_{i=1}^{n} x_i} \tag{2}$$

The relative range (R) was calculated as Eq. (3):

$$R = \frac{x_{\max} - x_{\min}}{\bar{x}} \tag{3}$$

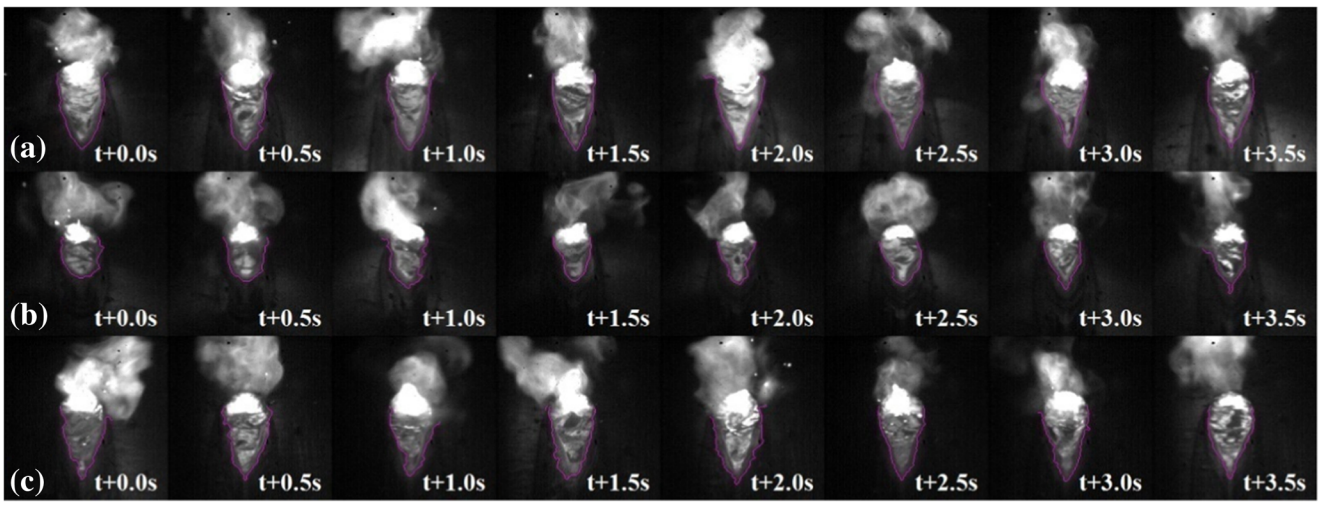

Fig. 8 Continuous images with different penetration status. **a** Group I. **b** Group II. **c** Group III

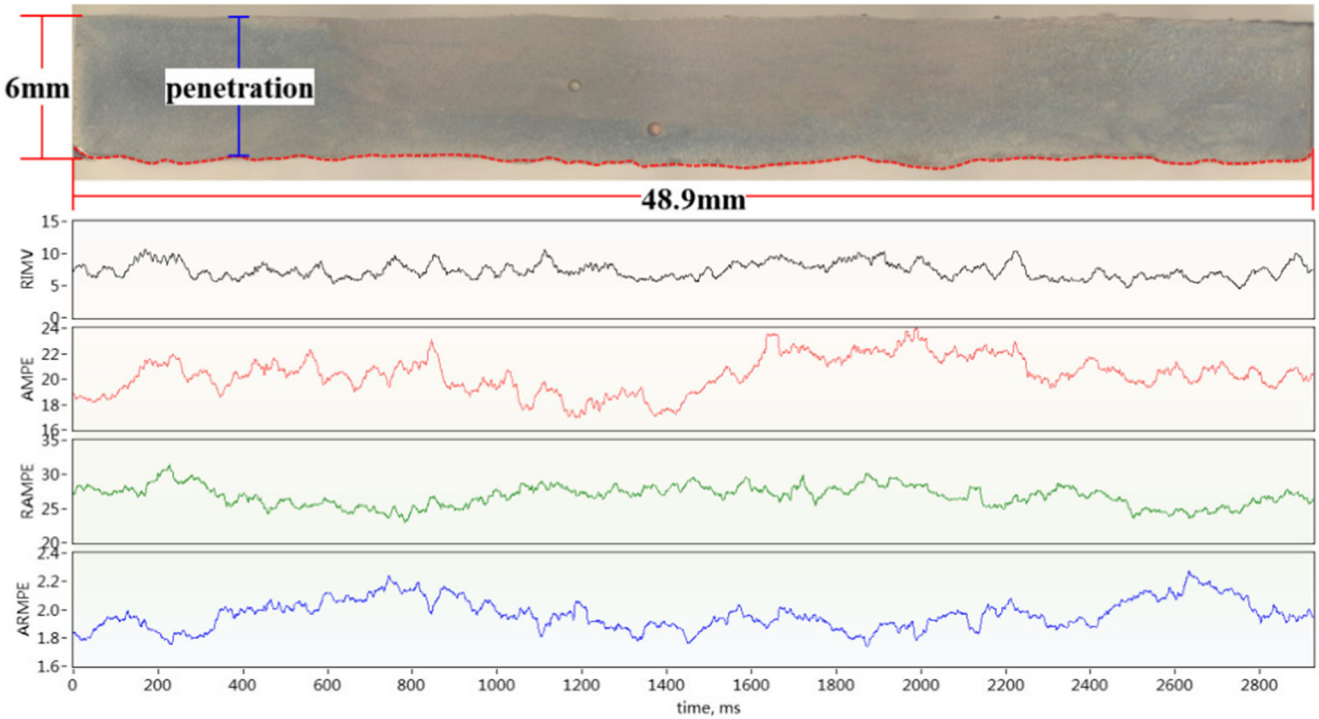

Fig. 9 The process parameters of full weld penetration (group I)

where $\bar{x}$ stands for the mean value of the group of data, x_{max} and x_{min} were the maximum and the minimum value of the this group, and n and s were the number and the standard deviation of the group. Normally, the smaller the variation coefficient and the relative range, the more stable the fluctuation is.

In the frequency domain, the dynamic information of image features could be extracted by Fourier transform, as shown

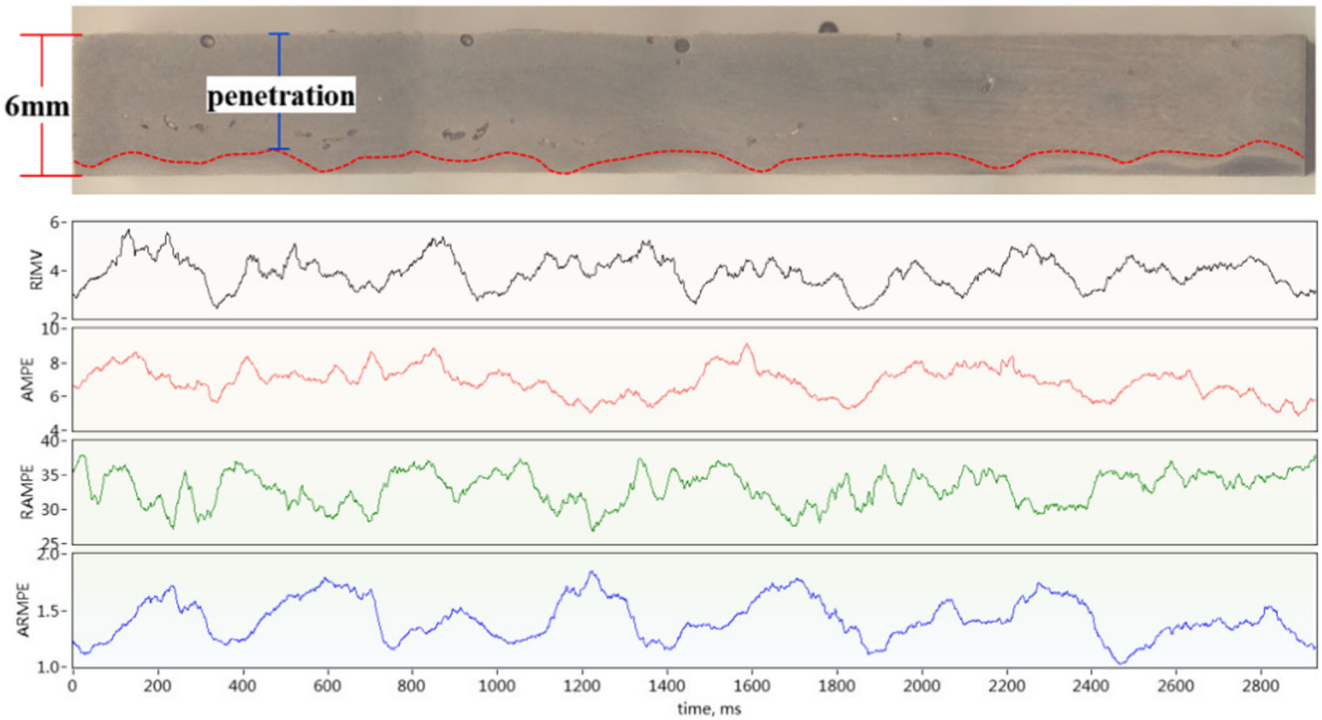

Fig. 10 The process parameters of partial weld penetration (group II)

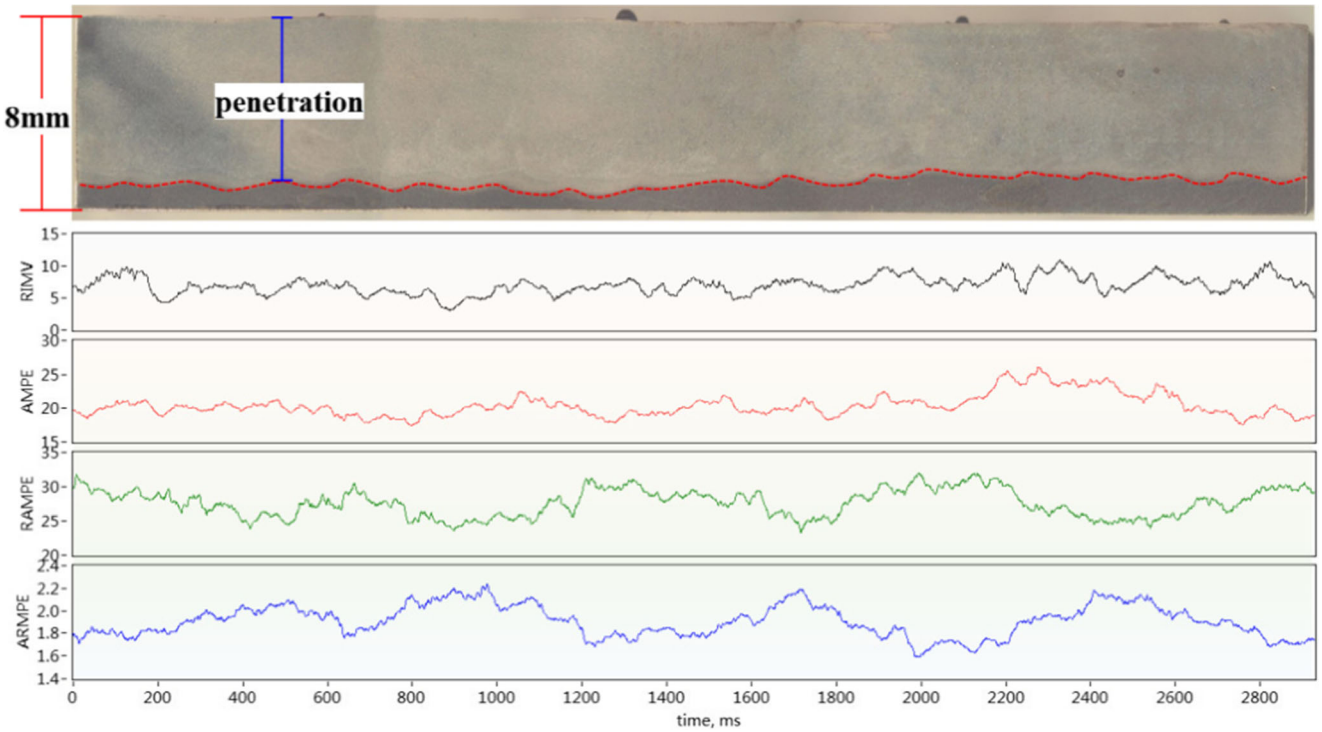

Fig. 11 The process parameters of partial weld penetration (group III)

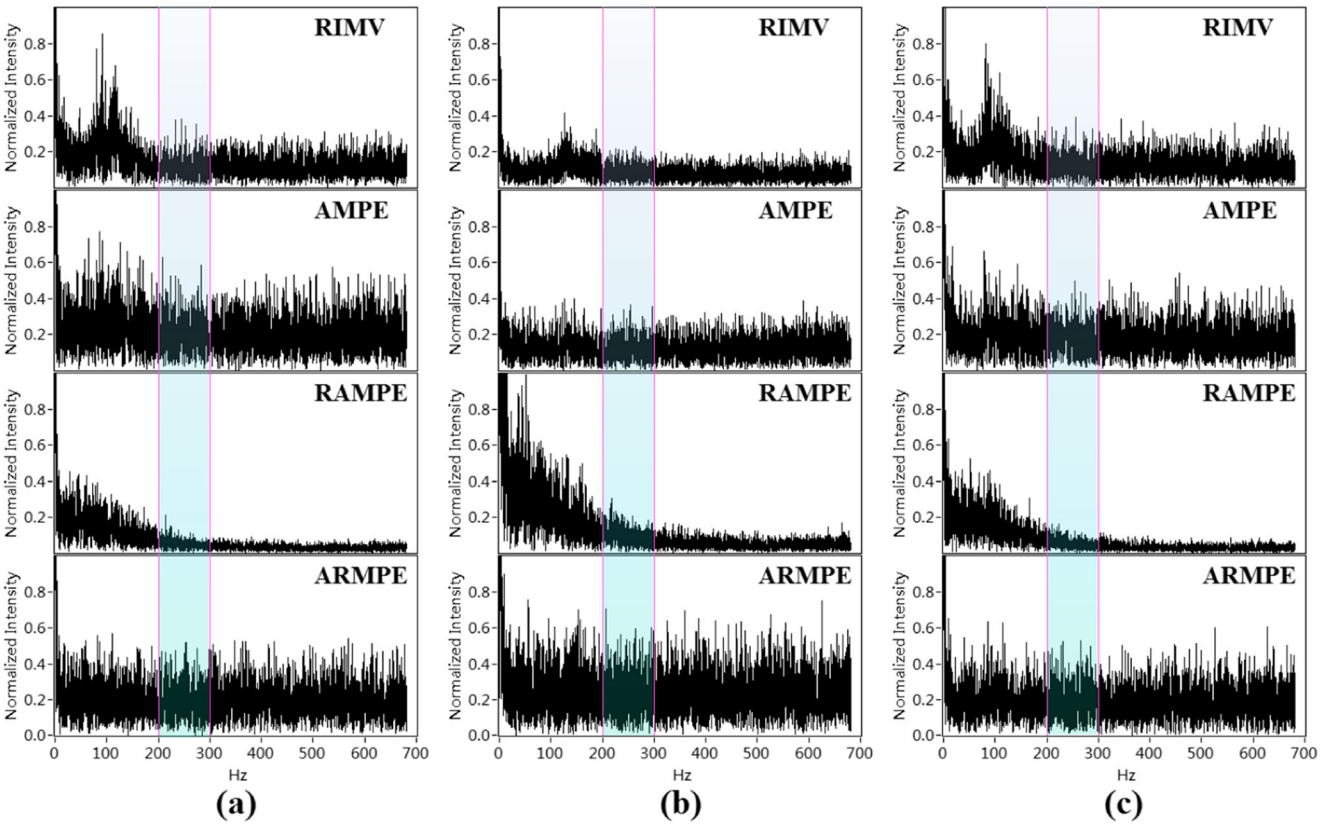

Fig. 12 The frequency distribution of image features with FFT transformation. **a** Group I. **b** Group II. **c** Group III

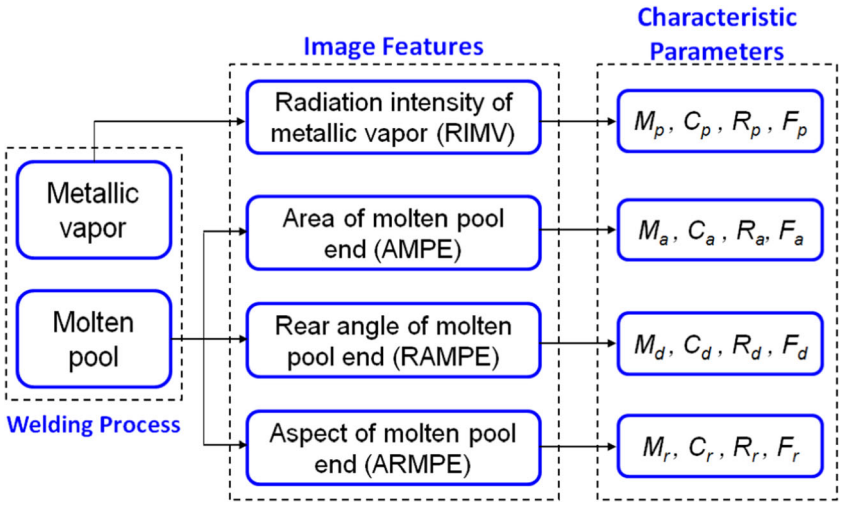

Fig. 13 The structure and extraction process of characteristic parameters

in Fig. 12. It could be observed that every feature had a significant low-frequency component, and the frequency was normally less than 10 Hz. It reflected the basic characteristics of molten pool and metallic vapor. However, the fluctuation of characteristic features caused by the keyhole condition was mainly reflected in the higher frequency band. The intrinsic frequency of metallic vapor, determined by the interaction between laser beam and welded material, mainly located in the range less than 200 Hz. On the other hand, the high frequency part was easy to be disturbed by external interferences. Accordingly, the distribution of characteristic features in the range of 200–300 Hz was used for the process analysis. In order to eliminate the influence of parameter dimension, the ratio between low-frequency part and 200–300 Hz part was calculated, as shown in Eq. (4):

$$F = \frac{k\int_{0}^{10} I_f df}{\int_{200}^{300} I_f df} = \frac{k\sum_{0}^{10} I_f}{\sum_{200}^{300} I_f} \tag{4}$$

where I_f was the intensity of the component with frequency f; k was constant.

In summary, there are four image features extracted from every image of molten pool and metallic vapor. Subsequently, the process characteristics of each feature were described by four process parameters. The mean

Table 1 Definition of the characteristic parameters as original variables for PCA

Original variables	Parameters	Definition
x_1	M_p	Mean value of metallic vapor's radiation intensity
x_2	F_p	Frequency ratio of metallic vapor's radiation intensity
x_3	C_p	Variation coefficients of metallic vapor's radiation intensity
x_4	R_p	Relative range of metallic vapor's radiation intensity
x_5	M_a	Mean value of molten pool end's area
x_6	F_a	Frequency ratio of molten pool end's area
x_7	C_a	Variation coefficients of molten pool end's area
x_8	R_a	Relative range of molten pool end's area
x_9	M_d	Mean value of molten pool end's rear angle
x_{10}	F_d	Frequency ratio of molten pool end's rear angle
x_{11}	C_d	Variation coefficients of molten pool end's rear angle
x_{12}	R_d	Relative range of molten pool end's rear angle
x_{13}	M_r	Mean value of molten pool end's aspect
x_{14}	F_r	Frequency ratio of molten pool end's aspect
x_{15}	C_r	Variation coefficients of molten pool end's aspect
x_{16}	R_r	Relative range of molten pool end's aspect

Table 2 The Correlation matrix in the case of laser power variation

	x_1	x_2	x_3	x_4	x_5	x_6	x_7	x_8	x_9	x_{10}	x_{11}	x_{12}	x_{13}	x_{14}	x_{15}	x_{16}
x_1	1.000	−0.887	−0.099	0.063	0.956	0.536	−0.064	−0.260	−0.879	0.233	0.019	−0.118	0.913	−0.560	−0.670	−0.783
x_2	−0.887	1.000	0.085	−0.011	−0.932	−0.443	0.030	0.271	0.877	−0.306	−0.189	−0.014	−0.899	0.470	0.503	0.651
x_3	−0.099	0.085	1.000	0.789	−0.149	0.099	0.316	0.286	0.149	−0.143	−0.152	−0.125	−0.143	0.037	0.050	0.070
x_4	0.063	−0.011	0.789	1.000	0.051	0.336	0.385	0.350	−0.048	0.041	−0.087	−0.121	0.058	−0.013	−0.027	−0.015
x_5	0.956	−0.932	−0.149	0.051	1.000	0.519	−0.067	−0.295	−0.968	0.281	0.063	−0.117	0.983	−0.567	−0.625	−0.749
x_6	0.536	−0.443	0.099	0.336	0.519	1.000	0.399	0.188	−0.467	0.080	0.000	−0.085	0.513	−0.397	−0.468	−0.608
x_7	−0.064	0.030	0.316	0.385	−0.067	0.399	1.000	0.896	0.111	0.227	0.370	0.313	−0.071	0.154	0.193	0.093
x_8	−0.260	0.271	0.286	0.350	−0.295	0.188	0.896	1.000	0.349	0.144	0.340	0.372	−0.307	0.266	0.345	0.317
x_9	−0.879	0.877	0.149	−0.048	−0.968	−0.467	0.111	0.349	1.000	−0.305	−0.017	0.181	−0.992	0.537	0.583	0.721
x_{10}	0.233	−0.306	−0.143	0.041	0.281	0.080	0.227	0.144	−0.305	1.000	0.646	0.417	0.277	0.590	0.380	0.200
x_{11}	0.019	−0.189	−0.152	−0.087	0.063	0.000	0.370	0.340	−0.017	0.646	1.000	0.764	0.047	0.509	0.596	0.361
x_{12}	−0.118	−0.014	−0.125	−0.121	−0.117	−0.085	0.313	0.372	0.181	0.417	0.764	1.000	−0.164	0.447	0.578	0.484
x_{13}	0.913	−0.899	−0.143	0.058	0.983	0.513	−0.071	−0.307	−0.992	0.277	0.047	−0.164	1.000	−0.562	−0.619	−0.760
x_{14}	−0.560	0.470	0.037	−0.013	−0.567	−0.397	0.154	0.266	0.537	0.590	0.509	0.447	−0.562	1.000	0.809	0.743
x_{15}	−0.670	0.503	0.050	−0.027	−0.625	−0.468	0.193	0.345	0.583	0.380	0.596	0.578	−0.619	0.809	1.000	0.904
x_{16}	−0.783	0.651	0.070	−0.015	−0.749	−0.608	0.093	0.317	0.721	0.200	0.361	0.484	−0.760	0.743	0.904	1.000

value (M), variation coefficient (CV), and relative range (R) were calculated based on statistical technology, and the frequency ratio (F) was designed in frequency domain. Accordingly, there were total 16 characteristic parameters for every weld. The parameter structure and extraction process were shown in Fig. 13. The group of process parameters provided abundant information of weld penetration. However, it is still difficult to judge the penetration state directly from the characteristic parameters. So, an effective method was necessary to integrate the information and provide a rapid and precise evaluation.

4 Detection method

4.1 Basic theory of principal component analysis

The foregoing 16 characteristic parameters, computed based on the images of molten pool and metallic vapor, provided plenty of information for the welding conditions. However, the information was not organized, and it is impractical to judge the penetration state directly. To this end, the principal component analysis (PCA) method was used to re-organize the parameters. Table 1 listed all the characteristic parameters as original variables for PCA.

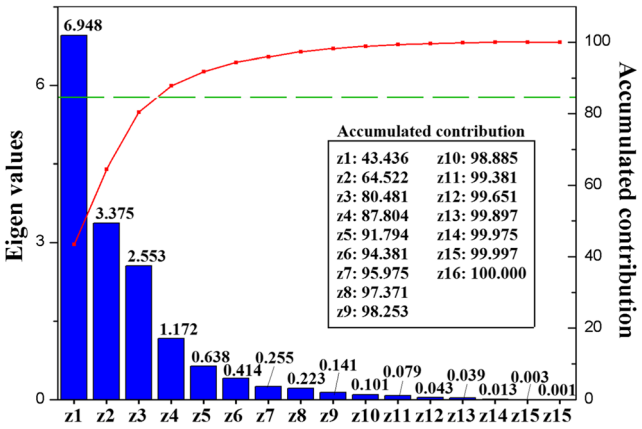

Fig. 14 Eigenvalues and accumulated contribution rate of principal components for varied power

PCA is a useful method to reduce the dimension of variables. The basic idea is to determine the primary and secondary position of the change direction according to the variance of the data variation, and the main components are obtained according to the order of primary and secondary.

Suppose the original variables are $x_1, x_2, \ldots, x_p$, the non-related principal components $z_1, z_2, \ldots, z_m$, as well as a complex indicator P, were extracted by the PCA method as the following steps:

A. To standardize the original variables for data unification.

$$x_{ki}^{*} = \frac{x_{ki} - \bar{x}_i}{\sqrt{S_{ii}^{*}}}, \quad k=1,2,\ldots,n; i=1,2,\ldots,m \tag{5}$$

where x_{ki}, $\bar{x}_i$, and S_{ii}^{*} are the original data, mean value, and standard deviation of variable x_i; x_{ki}^{*} is the standardized data.

B. To establish the correlation coefficient matrix.

$$R = \frac{1}{n-1} X^{*'} X^{*} \tag{6}$$

where X^{*} is the data matrix after standardization, and $X^{*'}$ is the corresponding transpose matrix.

C. To solve the characteristic equation for eigenvalues λ_i and eigenvectorsI_i.

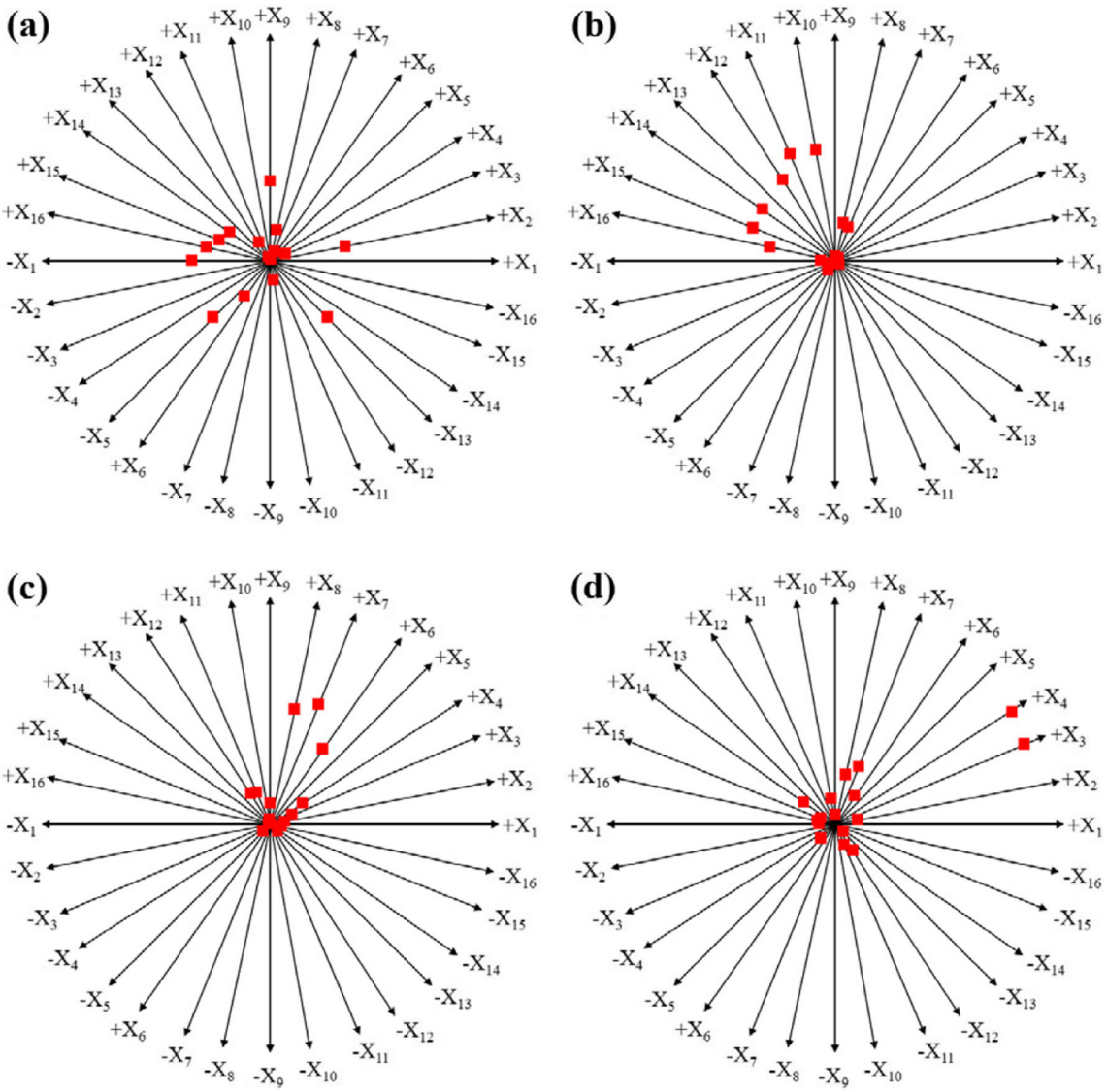

Fig. 15 The coefficient of principal components for varied power. **a** z_1. **b** z_2. **c** z_3. **d** z_4

The eigenvalue λ_i is calculated using the Jacob method. The number of principal components is determined when the accumulated variance contribution rate satisfies the condition:

$$\frac{\sum_{j=1}^{m}\lambda_j}{\sum_{j=1}^{P}\lambda_j}\geq 0.85, \text{or} \lambda_j \geq 1 \tag{7}$$

D. To transform the standardized indicators to principal componentsz_j.

$$z_j = X_i^{*T} b_j^0, j\in 1,2,...,m, i\in 1,2,...,p \tag{8}$$

E. To calculate the complex indicator based on the principal components.

The weight rate c_j of each principal component is the variance contribution rate:

$$c_j = \frac{\lambda_j}{\sum_{k=1}^{p}\lambda_k}, j\in 1,2,...,p \tag{9}$$

The weighted sum of the principal components is obtained:

$$Y = \sum_{k=1}^{m} c_j z_j, i\in 1,2,...,m \tag{10}$$

In this study, there were six welds in each group, and three computational sections were extracted from each weld, except the starting zone and ending zone. In average, the length of the computational section was 29 mm, and about 2333 frames were involved in each section. Totally, there were 54 computational sections

Table 3 The correlation matrix in the case of plate thickness variation

	x_1	x_2	x_3	x_4	x_5	x_6	x_7	x_8	x_9	x_{10}	x_{11}	x_{12}	x_{13}	x_{14}	x_{15}	x_{16}
x_1	1.000	0.428	−0.166	−0.038	0.708	−0.210	−0.470	−0.468	0.053	0.051	−0.354	−0.323	−0.117	−0.250	−0.416	−0.405
x_2	0.428	1.000	0.343	0.493	0.626	0.287	−0.344	−0.264	0.169	−0.348	−0.358	−0.396	−0.232	−0.344	−0.375	−0.335
x_3	−0.166	0.343	1.000	0.740	−0.117	0.099	0.113	0.123	0.318	−0.214	−0.074	−0.065	−0.333	−0.048	−0.100	−0.031
x_4	−0.038	0.493	0.740	1.000	0.101	0.270	0.188	0.205	0.328	−0.110	−0.024	−0.042	−0.320	0.019	−0.093	0.023
x_5	0.708	0.626	−0.117	0.101	1.000	−0.036	−0.607	−0.599	−0.044	−0.217	−0.427	−0.471	−0.041	−0.399	−0.465	−0.412
x_6	−0.210	0.287	0.099	0.270	−0.036	1.000	0.365	0.388	0.067	0.298	0.121	0.117	−0.066	0.232	0.140	0.191
x_7	−0.470	−0.344	0.113	0.188	−0.607	0.365	1.000	0.946	0.312	0.455	0.698	0.698	−0.219	0.493	0.685	0.727
x_8	−0.468	−0.264	0.123	0.205	−0.599	0.388	0.946	1.000	0.397	0.398	0.661	0.662	−0.294	0.479	0.662	0.710
x_9	0.053	0.169	0.318	0.328	−0.044	0.067	0.312	0.397	1.000	0.139	0.414	0.438	−0.982	0.305	0.407	0.458
x_{10}	0.051	−0.348	−0.214	−0.110	−0.217	0.298	0.455	0.398	0.139	1.000	0.553	0.402	−0.083	0.841	0.515	0.455
x_{11}	−0.354	−0.358	−0.074	−0.024	−0.427	0.121	0.698	0.661	0.414	0.553	1.000	0.913	−0.306	0.674	0.972	0.938
x_{12}	−0.323	−0.396	−0.065	−0.042	−0.471	0.117	0.698	0.662	0.438	0.402	0.913	1.000	−0.342	0.486	0.905	0.897
x_{13}	−0.117	−0.232	−0.333	−0.320	−0.041	−0.066	−0.219	−0.294	−0.982	−0.083	−0.306	−0.342	1.000	−0.214	−0.298	−0.353
x_{14}	−0.250	−0.344	−0.048	0.019	−0.399	0.232	0.493	0.479	0.305	0.841	0.674	0.486	−0.214	1.000	0.651	0.587
x_{15}	−0.416	−0.375	−0.100	−0.093	−0.465	0.140	0.685	0.662	0.407	0.515	0.972	0.905	−0.298	0.651	1.000	0.962
x_{16}	−0.405	−0.335	−0.031	0.023	−0.412	0.191	0.727	0.710	0.458	0.455	0.938	0.897	−0.353	0.587	0.962	1.000

uniformly from three experimental groups. Among them, two-thirds were used for training; the left one-third was used for verification.

4.2 Effects of laser power

The declination of laser power, caused by device malfunction or environmental disturbance, was a common reason for insufficient penetration. The condition was analyzed by a comparison between group I and group II. Therefore, there were total 36 sections, of which 24 sections were selected randomly for principal component analysis. The range of laser power was from 4 to 6 kW, and the plate thickness was from 6 to 8 mm. The correlation matrix was presented in Table 2. It could be observed that the correlation coefficients between many input variables, including x_1, x_2, x_5, x_9, and x_{13}, were very high. This indicated that the characteristic parameters carried the same information.

Eigenvalues of the principal components and their accumulated contribution rate were presented in Fig. 14. It could be seen that the accumulated contribution rate of the first four vectors was 87.804%, and the eigenvalue of the first four vectors were larger than 1, so the first four vectors were used as principal components to describe the welding process affected by the laser power.

The first four components could be calculated through the linear equation of all input variables. The coefficients of the input variables were between −1 and 1, and were presented in Fig. 15.

It could be observed that the first principal component z_1 had relatively similar loads on many input variables, including x_1, x_5, x_9, and x_{13}. The mean value of characteristic parameters had a high contribution to the first principal component. It indicated that some fundamental changes occurred on the molten pool and metallic vapor when incident laser power changed. As far as the other three principal components, they had a more obvious emphasis. The second principal component z_2 mainly focused on x_{10}–x_{16}, which indicated that the end morphology of molten pool carried a plenty of information. The principal component z_3 and z_4 concentrated on x_3–x_4 and x_7–x_8, respectively. Although the contribution of the two

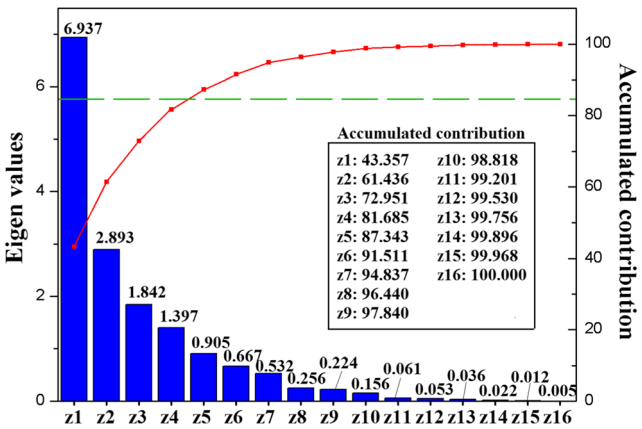

Fig. 16 Eigenvalues and accumulated contribution rate of principal components for varied thickness

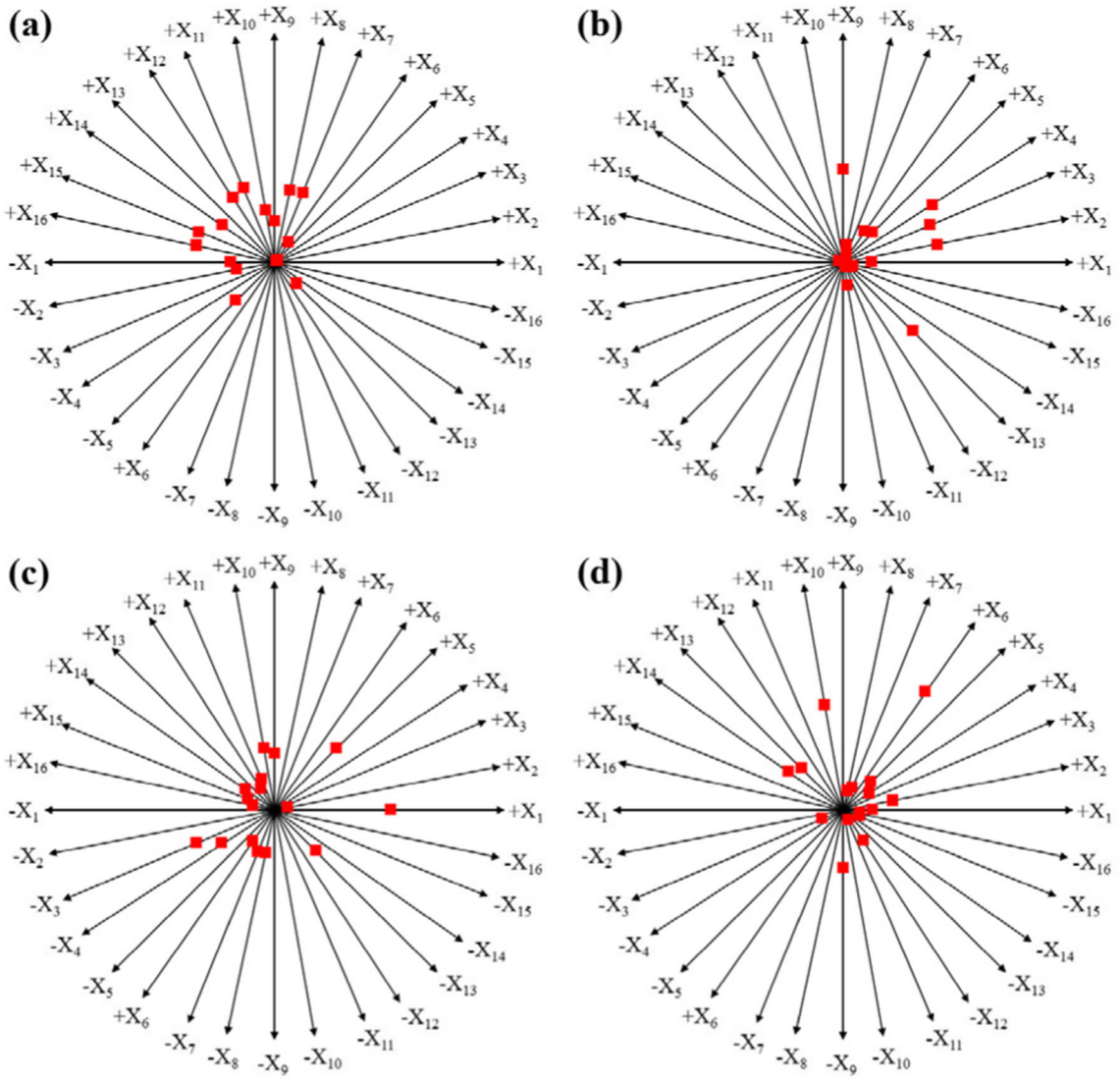

Fig. 17 The coefficient of principal components for varied thickness **a** z_1. **b** z_2. **c** z_3. **d** z_4

components was not as significant as the first two components, it showed that the behavior of molten pool and metallic vapor was also affected by the variation of incident laser.

$$Y_L = -0.139X_1 + 0.144X_2 + 0.151X_3 + 0.144_4 - 0.142X_5 - 0.037X_6 + 0.152X_7 + 0.178X_8 + 0.139X_9 + 0.096X_{10} + 0.120X_{11} + 0.119X_{12} - 0.140X_{13} + 0.191X_{14} + 0.199X_{15} + 0.189X_{16} \quad (11)$$

According to the first four principal components, the complex indicator was established as Eq. (11). The contributions from all characteristic parameters were relatively balanced. It indicated that the information carried by molten pool and metallic vapor, both in time domain and frequency domain, was helpful to recognize the penetration status under a varied laser power.

4.3 Effects of thickness variation

The comparison between group I and group III was carried out to investigate the lack of fusion caused by plate thickness. Similarly, there were total 36 sections, of which 24 sections were used for principal component analysis. The correlation matrix was shown in Table 3. Some pairs of input variables with correlation coefficients higher than 0.8 were found. But

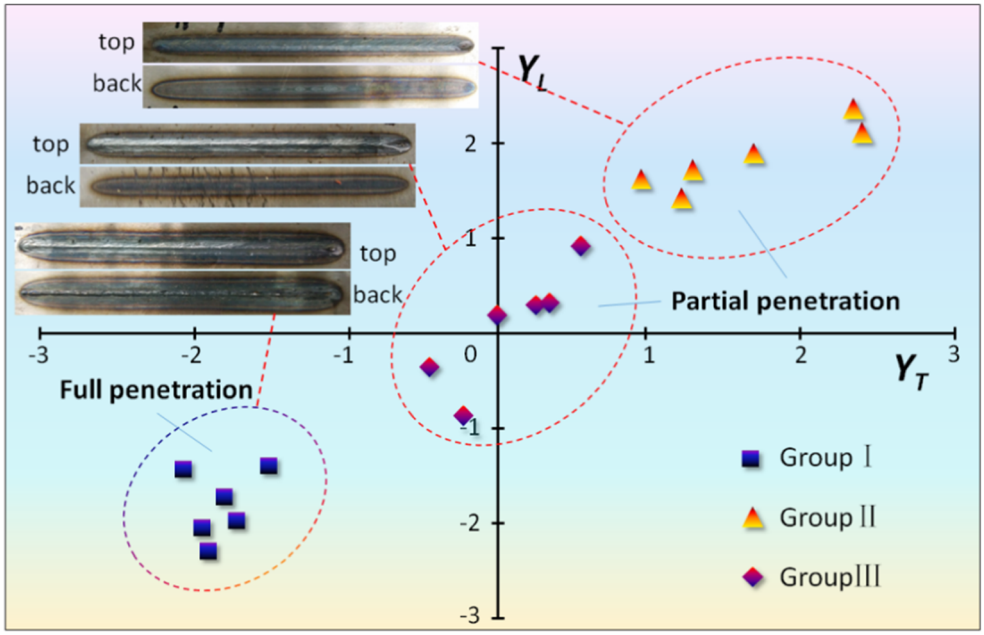

Fig. 18 The distribution of verification welds in the coordinate of complex indicators

the probability of this phenomenon was higher for x_{11} and x_{12}. It could be attributed to the differences of molten pool end caused by penetration status.

Figure 16 presented the eigenvalue and cumulated contribution rate of each principal component. It could be seen that the eigenvalues of the first four vectors were larger than 1, the accumulated contribution rate of the first four vectors was 81.685%, so the first four vectors are used as principal components. The formula for calculating the principal components using the standard data is presented in Fig. 17.

It could be observed that almost all input variables contributed obviously to the four principal components. In the overall point of view, it is difficult to evaluate the significance of input variables. Compared to group II, the differences of molten pool and metallic vapor in group III was obscure. The information from each variable was integrated to form the four principal components.

$$Y_T = 0.012X_1 + 0.034X_2 + 0.032X_3 + 0.087X_4 - 0.015X_5 + 0.133X_6 + 0.164X_7 + 0168X_8 + 0.192X_9 + 0.186X_{10} + 0.196X_{11} + 0.173X_{12} - 0.191X_{14} + 0.187X_{15} + 0.195X_{16} \quad (12)$$

According to the first four principal components, the complex indicator was established as Eq. (12). The coefficients of x_1–x_5 was obviously smaller than the other input variables. Among them, the first four parameters were derived from the image feature of metallic vapor. It could be inferred that the differences of metallic vapor was not significant when the power of incident laser was kept same. Relatively, the morphology of molten pool carried more information of penetration status in this case.

4.4 Verification results

Based on the principal component analysis executed on the foregoing two cases, two complex indicators, Y_L and Y_T, were obtained. In order to evaluate the effectiveness of the two indicators, the left 18 welds were used. Among them, half came from group II and half from group III. All welds that participated in the verification were not used in the previous modeling. During welding process, these welds were also observed, and the images of molten pool and metallic vapor were recorded by the same monitoring system. After welding, the complex indicators, Y_L and Y_T, were computed for every weld. The computed results and representative photos were listed in Fig. 18. The distribution of verification welds in the coordinate of complex indicators showed an ideal distinguishability. The six welds of group I were full-penetrated and centrally located in the third quadrant. The welds of other two groups scattered in the first quadrant or around the coordinate center. The gap between group I and the other groups ensured the reliability of the detection method. With the principal component analysis, the information of penetration carried by characteristic parameters was reorganized. The differences caused by penetration status were described to the most extent under the 2D coordinate of Y_L and Y_T.

As far as group II and group III, their distribution zones were close. The distances among some samples were very

short, although the distance between the far-ends was quite long. It might come down to the similarity of molten pool and metallic vapor in partial penetration mode. Although the cause of formation was not same, the two welding processes shared similar characteristics. Besides, the divergence of the two groups was remarkably higher than the first group. It indicated that the molten pool and metallic vapor were relatively instable in the case of partial penetration.

5 Conclusions

The weld penetration was determined by the keyhole depth for the welding process in deep penetration mode. For the plates with medium or big thickness, there were many interfering factors, including the fluctuation of laser power and workpiece thickness. Experimental results showed that the penetration state could be recognized on site through the morphology and the behavior of molten pool and metallic vapor. Accordingly, an effective and practical method was established based on image processing technology and principal component analysis. The effectiveness of the method has been demonstrated on the trial station of laser welding for automobile industries.

Generally, the following conclusions may be made:

1) The flow pattern mode of liquid metal behind the keyhole changed from double-circle mode to single-circle mode, when full penetration could not be maintained. At the same time, the radiation of metallic vapor on the top side of the workpiece was enhanced because the bottom outlet of the keyhole was closed. Accordingly, the morphology and behavior of molten pool and metallic vapor were affected. The images of molten pool and metallic vapor carried ample information of penetration status.
2) Four image features were extracted including the radiation intensity of metallic vapor (RIMV), the area of molten pool end (AMPE), the rear angle of molten pool end (RAMPE), and the aspect ratio of molten pool end (ARMPE). The statistical analysis and frequency domain analysis were carried out, and 16 characteristic parameters were computed for every weld. The differences of molten pool and metallic vapor caused by penetration status were described quantitatively.
3) The quantitative information of characteristic parameters was reorganized by the principal component analysis, in the case of laser power decreasing and the case of workpiece thickening. Two complex indicators were designed based on the principal components, respectively. Experimental results showed that the online detection method was effective to recognize the penetration status of a high-power laser welding.

Acknowledgements This work has been funded by the National Natural Science Foundation of China (Grant no. 51475297).

References

1. Bagger C, Olsen FO (2003) Laser welding closed-loop power control. Journal of Laser Applications 15(1):19–24
2. You D, Gao X, Katayama S (2015) Detection of imperfection formation in disk laser welding using multiple on-line measurements. J Mater Process Technol 219(219):209–220
3. Kim CH, Ahn DC (2012) Coaxial monitoring of keyhole during Yb:YAG laser welding. Optics & Laser Technology 44(6):1874–1880
4. Gao JQ, Qin GL, Yang JL, He JG, Zhang T, Wu CS (2011) Image processing of weld pool and keyhole in Nd: YAG laser welding of stainless steel based on visual sensing. Trans Nonferrous Metals Soc China 21(2):423–428
5. Zhang Y, Gao X (2014) Analysis of characteristics of molten pool using cast shadow during high-power disk laser welding. Int J Adv Manuf Technol 70:1979–1988
6. Luo M, Shin YC (2015) Vision-based weld pool boundary extraction and width measurement during keyhole fiber laser welding. Optics & Lasers in Engineering 64(12):59–70
7. Oezmert A, Drenker A, Nazery V (2014) Detectability of penetration based on weld pool geometry and process emission spectrum in laser welding of copper. Proceedings of SPIE - The International Society for Optical Engineering 41:509–514
8. Kratzsch C, Abels P, Kaierle S, Poprawe R, Schulz W (2000) Coaxial process control during laser beam welding of tailored blanks. Proceedings of SPIE - The International Society for Optical Engineering 3888:472–482
9. Abt F, Blug A, Nicolosi L, Dausinger F, Höfler H, Tetzlaff R, Weber R (2009) Real time closed loop control of full penetration keyhole welding with cellular neural network cameras. Journal of Laser Micro Nanoengineering 6(2):131–137
10. Blug A, Carl D, Höfler H, Abt F, Heider A, Weber R, Nicolosi L, Tetzlaff R (2011) Closed-loop control of laser power using the full penetration hole image feature in aluminum welding processes. Phys Procedia 12(Part 1):720–729
11. Shidfar A, Alinejadmofrad M, Garshasbi M (2009) A numerical procedure for estimation of the melt depth in laser material processing. Optics & Laser Technology 41(3):280–284
12. Courtois M, Carin M, Masson P L, Gaied S, Balabane M (2013) A new approach to compute multi-reflections of laser beam in a keyhole for heat transfer and fluid flow modelling in laser welding. Journal of Physics D Applied Physics, 46(50)
13. Li S, Chen G, Zhou C (2015) Effects of welding parameters on weld geometry during high-power laser welding of thick plate. Int J Adv Manuf Technol 79(1–4):177–182
14. Tan W, Bailey NS, Shin YC (2013) Investigation of keyhole plume and molten pool based on a three-dimensional dynamic model with sharp interface formulation. Journal of Physics D Applied Physics 46(5):55501–55512(12)
15. Fabbro R (2010) Melt pool and keyhole behaviour analysis for deep penetration laser welding. Journal of Physics D Applied Physics 43(44):573–580